Materials Chemistry and Physics 223 (2019) 727–736

Contents lists available at ScienceDirect

Materials Chemistry and Physics

journal homepage: www.elsevier.com/locate/matchemphys

Induction periods during anodic polarization of zinc in aqueous oxalic acid solutions

E. Lilov[a], V. Lilova[a], Ch. Girginov[a], S. Kozhukharov[b,*], A. Tsanev[c], D. Yancheva[d]

[a] Faculty of Chemical Technologies, University of Chemical Technology and Metallurgy, 8 Kliment Ohridski blvd., 1756, Sofia, Bulgaria
[b] LAMAR-Laboratory for Advanced Materials Research, University of Chemical Technology and Metallurgy, 8 Kliment Ohridski blvd., 1756, Sofia, Bulgaria
[c] Institute of General and Inorganic Chemistry, Bulgarian Academy of Sciences, Acad. G. Bonchev str., building 11, 1113, Sofia, Bulgaria
[d] Institute of Organic Chemistry with Centre of Phytochemistry, Bulgarian Academy of Sciences, Acad. G. Bonchev str., building 9, 1113, Sofia, Bulgaria

HIGHLIGHTS

- Anodic galvanostatic polarizations are performed on pure Zn in oxalic acid solutions.
- The acid concentrations and the current densities were varied in large ranges.
- Distinguishable induction periods were registered in all the investigated cases.
- A conceptual model is created for explication of the investigated systems behavior.
- The proposed model was verified by the experimental results.

GRAPHICAL ABSTRACT

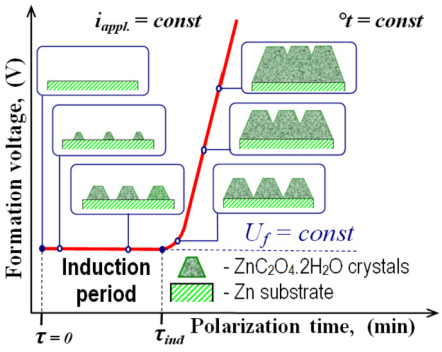

ARTICLE INFO

Keywords:
Zinc
Oxalic acid
Induction periods
Anodic polarization

ABSTRACT

The anodic polarization of zinc in aqueous solutions of oxalic acid was investigated. The polarizations were carried out in electrolytes with concentrations between 0.005 and 0.500 mol dm^{-3}, at constant current densities (1 ÷ 40 mA cm^{-2}). In the course of anodic polarization, induction periods were distinctly recorded, and their durations were found to be strongly dependent on both the electrolyte concentration and the applied current density. By employing XPS and XRD diffraction methods and performing ATR-FTIR measurements, it was established that the layers formed on the metal surface are composed of crystalline zinc oxalate dihydrate, covered with thin ZnO external layers. Furthermore, a conceptual model was developed which qualitatively explains the mechanism of appearance of the observed induction periods. This model perceives the roughness variation of the electrode surface during anodic polarization. The obtained AFM images and SEM micrographs confirm the assumptions made in the presented model. During the polarization of zinc in aqueous solutions of oxalic acid, high voltages are reached, which makes them suitable for forming $ZnC_2O_4.2H_2O$ coatings.

1. Introduction

The great interest towards ZnO-based materials, is predetermined by their unique optical and electrical properties [1,2]. Besides for further extension of the durability of corrosion protective zincate coatings [3–10], the ZnO-based materials have recently been examined for other attractive applications, such as alternative energy sources like solar elements [11–15], fuel cells [16–19], environmental monitoring

* Corresponding author.
E-mail addresses: stephko1980@abv.bg, stefko1980@abv.bg (S. Kozhukharov).

https://doi.org/10.1016/j.matchemphys.2018.11.044
Received 23 August 2018; Received in revised form 11 November 2018; Accepted 17 November 2018
Available online 19 November 2018
0254-0584/

sensors [20–23], optical components [24–26], pollutant removal catalysts [27–30], etc.

On the other hand, the electrochemical methods enable relatively facile synthesis with easily controllable conditions, providing high reproducibility of the product's characteristics using relatively simple equipment. The behavior of zinc during anodic polarization is assessed in a large variety of liquid media. Thus, various, mostly aqueous solutions were used as contact electrolytes, such as: bicarbonate electrolytes [31–33], NaOH [34,35], KOH [36], $KHCO_3$ [37], alkalized NaCl solutions [38], saturated zincate solutions [39], sodium oxalate [40], several baths with complex compositions, containing NaOH, $Na_2B_2O_7.10H_2O$, $Na_2Si_2O_3.9H_2O$, $NaNO_2$ and $NiSO_4$ [41] and even deionized water [42]. Also, methanolic solutions of lithium perchlorate [43], ethanolic H_2SO_4 solutions [44], fluoride containing 2-methyl-1,3-propandiol electrolyte [45], different electrolytes containing F^- ions [1,12–14] were used, too.

The majority of the research papers investigating the anodic behavior of Zn report its potentiostatic anodic polarization (2 ÷ 30 V) except for [34], where both galvanostatic and potentiostatic regimes were used. Almost all authors preferred to perform experiments at room temperature aside from Ref. [45], where the temperature was varied in the interval from −2 to +30 °C. The anodic polarization of zinc results in the obtaining of complex structures consisting of oxides, oxalates, phosphates, fluorides and others [31–49].

Particularly, zinc oxalate nanoparticles with different shapes and sizes were electrochemically synthesized by anodic polarization of zinc substrates in aqueous sodium oxalate solutions. It was found that their shapes and dimensions could be controlled by varying the cell voltage, oxalate ion concentration, and the stirring rate of the electrolyte [40]. Thus, porous films [31,46,48,50], structures with nanowires [34,37,46], nano-flakes [51] and nanospheres [45] have already been obtained. Other structures, consisting of bundles of nanowires [31,32,47], self-assembled stripe arrays of zinc oxides [44] and highly oriented ZnO nano-needle arrays [39] have also been observed.

The anodic polarization of Zn in aqueous oxalic acid solutions with different concentrations has been studied [52–54], as well. Furthermore, it was established that the anodic polarization of Zn in $Na_2C_2O_4$ aqueous solutions (0.01 ÷ 0.10 M), at a constant voltage (2 ÷ 8 V) results in the formation of zinc oxalate (ZnC_2O_4) crystals on the metallic surface [40]. The authors have succeeded to establish a proportional relation between the electrolyte concentration and the resulting ZnC_2O_4 particles grain size.

All these research activities and the established correlations therein have imposed the need for extended systematical elucidation of the Zn/$C_2H_2O_4$ system behavior during anodic polarization in relatively wide ranges of oxalic acid concentrations and current densities. This approach has enabled detailed assessment of the correlations between the anodic polarization conditions and the resulting features of the obtained films. In addition, a conceptual model was created on the basis of the further analysis of the obtained data.

2. Experimental

2.1. Sample preparation

Electrodes with a working area of 2 cm^2 were cut out from pure (99.98%) zinc foil. The working surfaces were electrochemically polished for 15 min in a mixed solution of phosphoric acid and ethanol (volume ratio 3:7) at a temperature of 5 °C [4], and the specimens were then rinsed with double-distilled water.

The anodic polarization was carried out in a standard two electrode cell with a golden cathode. The process was performed at galvanostatic, isothermal (20 °C) conditions for different durations. The simultaneous *in-situ* recording of the curve enabled to determine the film forming voltage (U_f) with time (t), respectively, with the total charge passed (Q). The applied current density (J) was varied from 1.25 to 40.00 mA cm^{-2}. Various $C_2H_2O_4$ solutions in the concentration range between 0.005 and 0.500 M were used as forming electrolytes. The electrolytes were not stirred, in order to avoid any influence of hydrodynamic effects.

2.2. Film characterizations

In order to determine the impact of the current density and the electrolyte concentration on the resulting films' structure, composition and morphology, the obtained anodic films were characterized using four advanced analytical methods, as follows:

2.2.1. Compositional analysis

The chemical composition of the films was determined by X-ray Photoemission Spectroscopy (XPS) and Attenuated Total Reflection-Fourier Transform Infrared (ATR-FTIR). The XPS spectra were acquired by AXIS Supra electron spectrometer (Kratos Analytical Ltd.) using monochromatic AlKα radiation with a photon energy of 1486.6 eV. The FTIR spectra were recorded on a Brueker Tensor 27 FT spectrometer, equipped with a diamond crystal ATR accessory, accumulating 64 scans at a resolution of 2 cm^{-1}.

2.2.2. Structural characterization

X-ray diffraction (XRD) patterns for phase identification were recorded in the angle interval 10-95°(2θ), on a Philips PW 1050 diffractometer, equipped with CuKα tube and scintillation detector.

2.2.3. Morphological description

The morphology of the samples was observed by Scanning Electron Microscopy (SEM). A Tescan SEM/FIB LYRA I XMU device with a secondary electrons detector was used at 25 000× magnification rate.

2.2.4. Topological observations

Atomic Force Microscopy (AFM) observations were performed, using Easyscan 2 by "Nanosurf" (Switzerland) equipped with TAP 190-G cantilever on square zones with linear size of 20 μm, at 256 points per line and 256 lines of resolution. The speed was 5 s per line, operating in continuous, dynamic regime at 17 kHz and 800 mV amplitude of cantilever vibration.

3. Results and discussion

3.1. Kinetic studies

3.1.1. Impact of the electrolyte concentration

It is well known, that during galvanostatic anodic polarization of various metals, alloys and semiconductors, the formation voltage (U_f) increases with time (t), respectively with the total electric charge passed (Q). This observation is a direct consequence of the increase of the formed film's thickness and its respective electrical resistance.

$U_f(t)$-kinetic curves were acquired during the anodic polarization of zinc in $C_2H_4O_4$ solutions in a large range of concentrations. Appearance of induction periods was established for the entire investigated concentration interval (0.005 ÷ 0.500 M). An illustration of these induction periods is represented in the kinetic curves, acquired at constant current density (5 mA cm^{-2}) for 0.005, 0.010 and 0.250 mol dm^{-3} (Fig. 1).

The data presented in Fig. 1 allow the following conclusions to be drawn: (i) The anodic polarization of Zn in oxalic acid solutions could reach rather high voltages (above 100 V); (ii) The induction period duration (τ_{ind}) decreases with increasing electrolyte concentrations.

It is noteworthy, that the (τ_{ind}) values reveal a stochastic character for all investigated electrolyte concentrations (Fig. 2). The results obtained from 6 individual experiments for each of the investigated concentrations have enabled to statistically estimate the most probable (τ_{ind}) value.

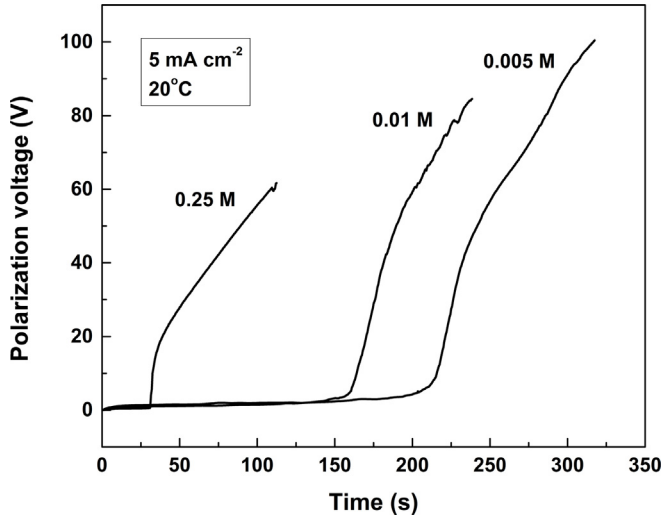

Fig. 1. Typical $U_f(t)$- kinetic curves for anodic polarization of zinc in aqueous solutions of oxalic acid.

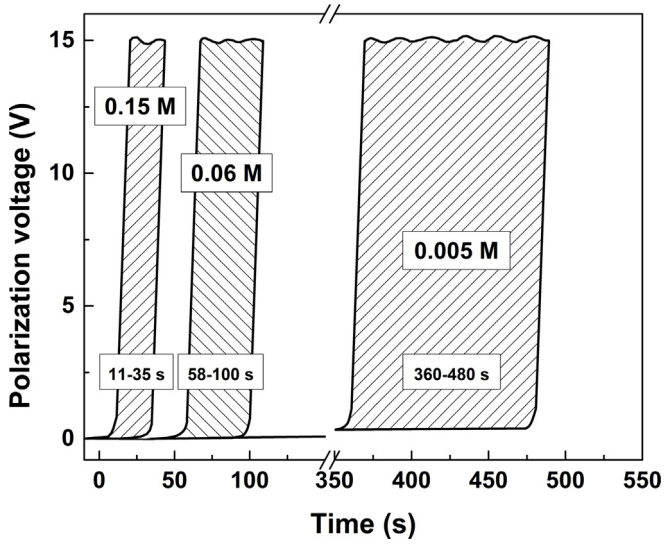

Fig. 2. Illustration of the induction period duration (τ_{ind}) confidence intervals for three different oxalic acid concentrations.

Thus, it was established that the standard deviation decreases for higher electrolyte concentrations. Since the crystallite's nucleation possesses a stochastic character, the film formation on each sample initiates with a different number of nuclei. The notably larger dissipation of the induction period durations, observed at lower concentrations is related to the fewer nuclei, being formed in these cases. Thus, the appearance of each new crystallite has a more considerable contribution to the duration of the induction period (τ_{ind}), correlated to the total number of nuclei. When this number is eventually large enough, the contribution of each crystal nucleus becomes indistinguishable and consequently the dissipations of the induction periods approach a defined average value, closer to each other.

The $\tau_{ind}(C)$-dependence, determined at 5 mA cm^{-2} and 20 °C for all investigated electrolytes is illustrated in Fig. 3.

The experiments reveal that the lowest possible concentration which enables a layer formation on zinc at 5 mA cm^{-2} is 0.005 mol dm^{-3}. Between this concentration and 0.150 M, the duration of the induction period strongly decreases and then reaches a plateau. Obviously, at the lower concentrations, the electrochemical film formation is retained by diffusion limitations, originating from the hindered delivery of oxalate ions to the metallic surface. Namely for this

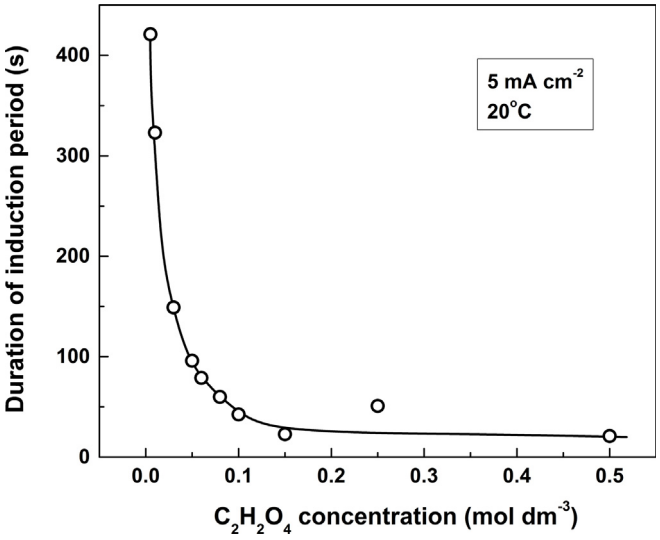

Fig. 3. Dependence of the induction period duration (τ_{ind}) on the electrolyte concentration.(C)

reason the concentration interval between 0.005 and 0.150 mol dm^{-3} was submitted to a detailed investigation in the present study.

3.1.2. Impact of the current density

The applied current density (J) has a considerable influence on the duration of the induction periods. This dependence, determined for 0.060 M oxalic acid, is illustrated in Fig. 4.

The analysis of the experimental data has revealed a decrement of the induction period duration, as well as its deviations (determined from 6 independent measurements for each data point) with higher applied current densities for all investigated electrolyte concentrations. The occurrence of induction periods has already been registered during the anodic polarization of various metals (Ta [55], Bi [56], Sb [57], Mo [58,59]). Similar $\tau_{ind}(J)$-dependences have been observed during the anodization of these metals in different electrolytes [55–59]. Besides, higher current densities lead to lower deviations in (τ_{ind}).

3.2. Film characterization

As it was already mentioned, the phase composition of the resulting

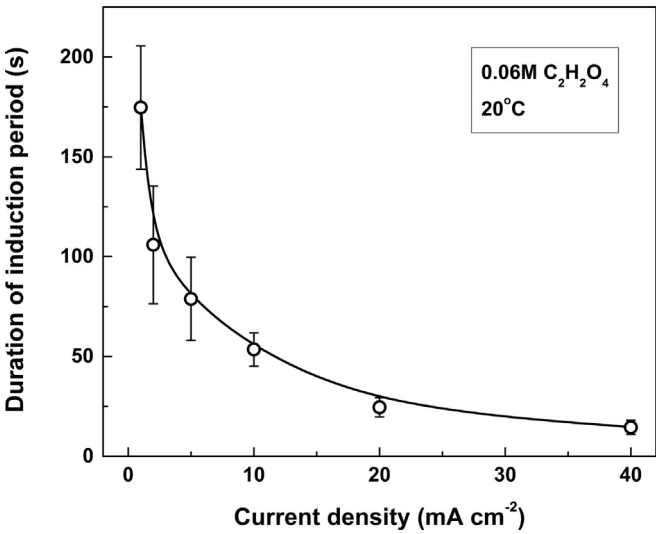

Fig. 4. Dependence of the induction period duration (τ_{ind}) on applied current density (J) for Zn polarized in 0.060 M oxalic acid.

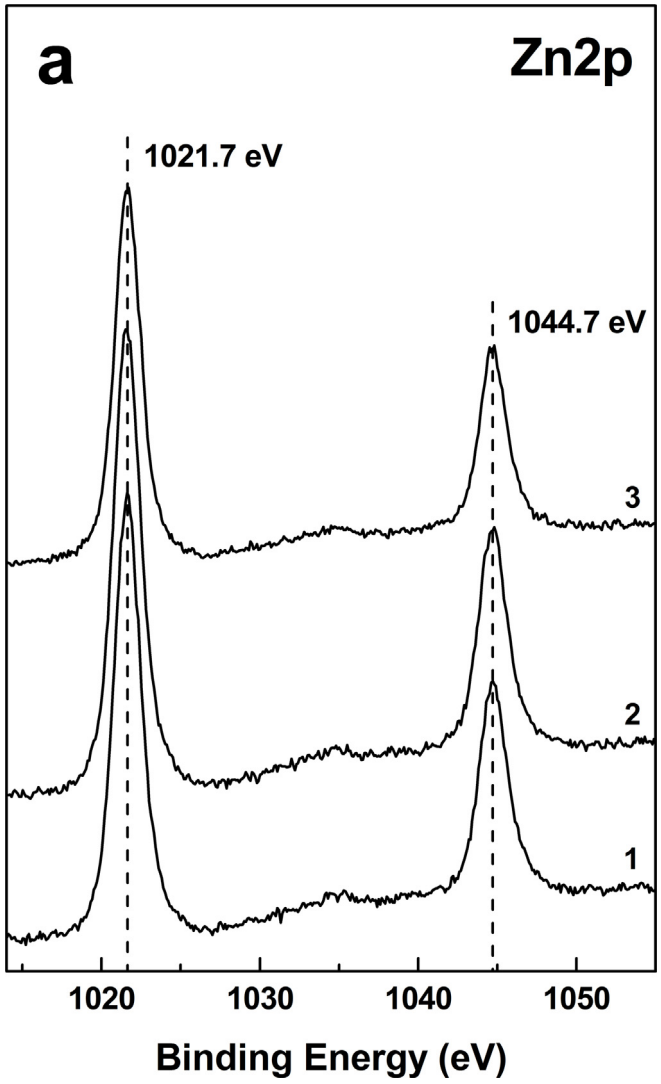

Fig. 5. Integral Zn2p (a) and Zn LMM (b) spectra of ZnC_2O_4 films obtained by anodic polarization at 5 mA cm^{-2} of three samples polarized in: (1) 0.005 M, (2) 0.060 M and (3) 0.150 M oxalic acid.

surface layers is strongly dependent on the composition of the used anodizing (contact) electrolyte [31–49]. In this sense, the chemical composition of the obtained films, formed in oxalic acid medium was an object of interest, as well. The modified surfaces of the samples were characterized by two analytical methods and the results are described below.

3.2.1. X-ray Photoemission Spectroscopy (XPS)

This method has enabled to define the chemical composition on the surface of the obtained films. For this purpose, three representative samples, undergone anodic polarization at constant current density (5 mA cm^{-2}) in three different electrolyte concentrations: 0.005; 0.060 and 0.150 mol dm^{-3}, were submitted to XPS analysis and the obtained Zn2p and Zn LMM spectra are shown in Fig. 5.

The anodic polarizations of the samples, submitted to XPS analysis were extended until the end of the respective induction periods, in order to guarantee continuous Zn-oxalate films. Fig. 5a shows Zn2p spectra, which are typical for this chemical element with a peak for $Zn2p_{3/2}$ at 1021.7 eV and a significant spin-orbit splitting from 23 eV. Since it is difficult to estimate the chemical state only from Zn2p spectra [60], it was necessary to acquire Zn LMM spectra (Fig. 5b), as well. The occurrence of Zn2p spectra, Auger spectra and the value of the modified

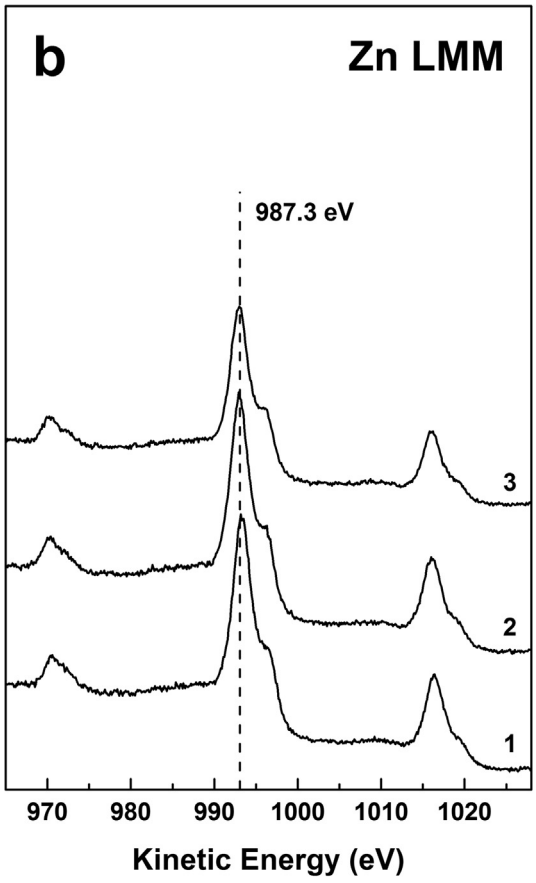

Fig. 5. (*continued*)

Auger parameter (2009 eV) are all characteristic for ZnO [61].

The further O1s spectra of the samples, shown in Fig. 6a were acquired in order to define the exact composition of the obtained films.

The obtained single peak is narrow and symmetric, confirming the presence of only Zn-compounds in the formed films. Although the positions of the O1s peaks for ZnO [62] and $Zn(CH_3COO)_2.2H_2O$ [63] are indistinguishable from each other, being at the same energy (531.6 eV), it was possible to differentiate these compounds (i.e. oxide and oxalate), from the area of the C1s peak, associated with COO^-–groups.

The acquired patterns (Fig. 6b) are broad and consist of two wide peaks. These spectra were deconvoluted in order to extract the values of areas for all components of carbon. The fits used for data extraction for the C-C and C-O bonding configurations and their intensities are indicated in Fig. 6. The peaks were fitted using 100% Lorentzian distribution, after performing a Shirley background subtraction. The fitting procedure was performed by fixing of the full width at half maximum (FWHM) values at 1.9 eV for all peaks. All peaks were then fitted to four components. The component at 284.2 eV originates from the graphitic sp^2 carbon. The peak at 285.9 eV is identified as C-atoms, directly bonded to oxygen in oxide or hydroxyl groups. The peak at 290.2 eV belongs to the carbon in carboxyl groups [64,65]. The π-plasmon peak is ascribed to π–π* transitions, which are characteristic for aromatic ring structures [66].

Table 1 summarizes the contents of the components, composing the surface of the obtained films. The last column shows that the ratio between oxygen and zinc is lower (i.e. O:Zn = 3:1) than the expected value for zinc oxalate (i.e. O:Zn = 4:1). The reason for this deviation in the elemental content from the expected stoichiometry is the contribution of ZnO, which is evinced by the Auger-spectra of Zn (i.e. Zn–LMM in Fig. 5b). Furthermore, the modified Auger-spectrum pattern is typical for ZnO, excluding the occurrence of other Zn-containing compounds, e.g. $ZnCO_3$. According to the area, normalized in relation

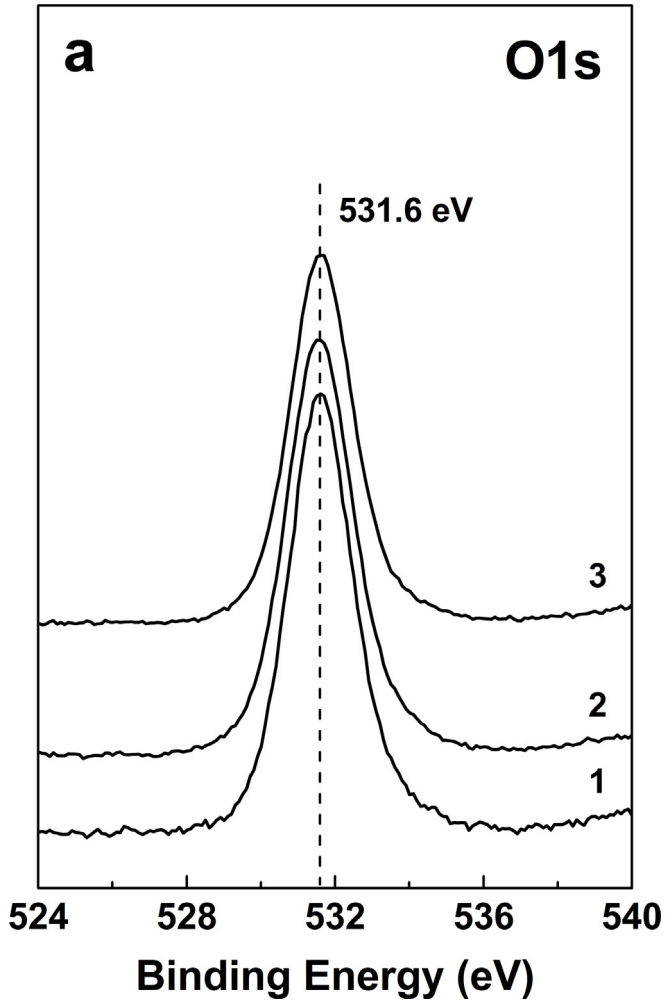

Fig. 6. C1s spectra of Zn anodically polarized at constant current density (5 mA cm^{-2}) until 37 V: (1) 0.005 M, (2) 0.060 M and (3) 0.150 M $C_2H_2O_4$.

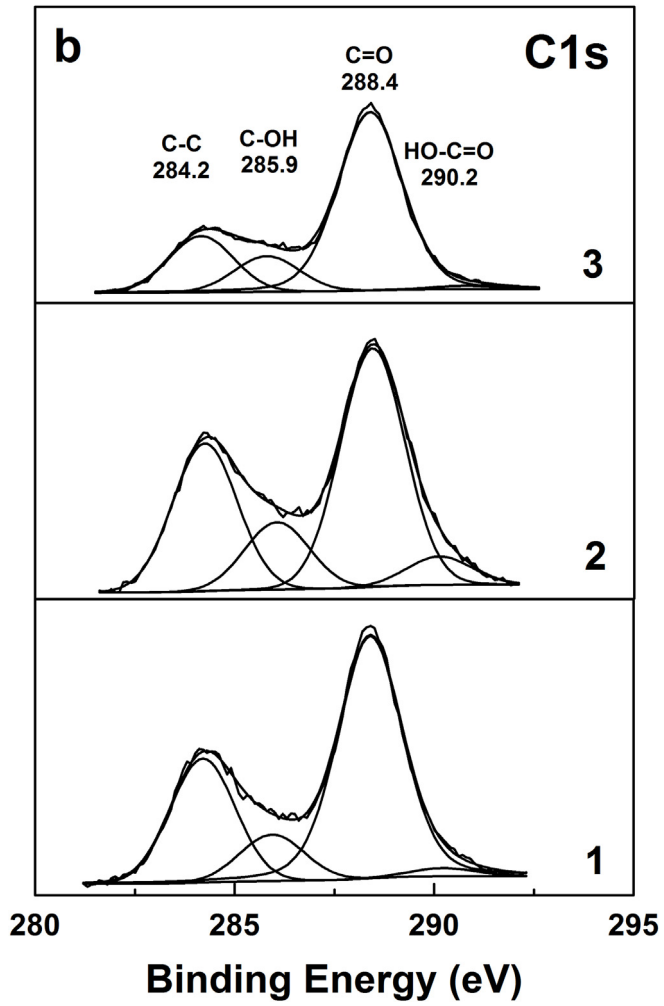

Fig. 6. (*continued*)

to the values of the Relative Sensitivity Factors (RSF), the correlation of the C1s (290.2 eV, Fig. 6b) peak area related to the COO^{-}-moieties, to this of the $Zn2p_{3/2}$ – peak for the respective samples in Table 1 reveals that these correlations are 0.05:0.15:0.03, respectively. This finding reveals a remarkable predominance of ZnO being about 96–97%, compared to only 3–4% of ZnC_2O_4.

Consequently, according to the XPS analyses the Zn-oxalate films are covered by a ZnO layer.

3.2.2. X-ray diffraction (XRD) measurements

This method has enabled to perform a phase identification of the obtained structures in the film bulk. The XRD diffraction patterns of sample, polarized in 0.005, 0.060 and 0.150 M $C_2H_2O_4$ solutions at a constant current density (5 mA cm^{-2}), up to 37 V, is presented in Fig. 7.

A High rate of crystallinity was registered in the structure of the investigated specimens. Two phases were identified: zinc oxalate (ZnC_2O_4) [67] and pure metallic zinc [68,69]. The presence of the metallic zinc peaks is most likely due to the contribution of the substrate.

3.2.3. ATR-FTIR measurements

The chemical composition of all obtained films was also determined by acquisition of their ATR-FTIR spectra. For illustration, the spectra of two of the investigated samples are depicted in Fig. 8. For comparison, a typical spectrum of Zn oxalate dihydrate ($ZnC_2O_4.2H_2O$) is represented as well.

Fig. 8 reveals that the ATR spectra of the studied samples are in excellent agreement with those of the reference Zn oxalate dihydrate. Following the reported assignments of the characteristic IR absorptions of zinc oxalate [40,54–63,67–72] and references therein, the bands in the region 4000-600 cm^{-1} of the spectra of anodized samples should be attributed to: 3380 cm^{-1} (O-H stretching), 1620 cm^{-1} (asymmetric C-O stretching), 1361 and 1316 cm^{-1} (symmetric C–O stretching + O–C–O bending), 819 cm^{-1} (symmetric C–C stretching coupled with O–C–O bending), 737 cm^{-1} (O-H rocking). In accordance with previous studies on hydrated metal oxalates, a band for the bending O-H mode of water was not observed due to overlapping with the strong IR band of the asymmetric C-O stretching vibrations at 1620 cm^{-1}.

The results obtained from both analytical methods used have undoubtedly evinced that the films formed by anodic polarization of Zn in oxalic acid obviously consist of crystalline zinc oxalate dihydrate.

3.3. Conceptual model regarding the origin of the induction periods

3.3.1. Correlation between the shape of the kinetic curve and the resulting morphological alterations

An attempt to explain the occurrence of the detected induction periods was made in the present study. For this purpose, the sample surfaces were submitted to systematical observations via Scanning Electron Microscopy (SEM) and Atomic Force Microscopy (AFM). In order to get a better understanding, an analysis of Fig. 9 is performed. It represents a kinetic $U_f(t)$ curve for the anodic polarization of zinc in 0.06 M oxalic acid at 5 mA cm^{-2}.

Table 1
Surface composition of the films at obtained 5 mA cm^{-2} as a function of electrolyte concentration.

Electrolyte concentration	Component C ($\%_{at}$)	Component O ($\%_{at}$)	Component Zn ($\%_{at}$)	Content of Zn-oxalate on the ZnO surfaces (%)
0.005 M	39.10	46.20	14.70	3.4
0.060 M	38.00	46.10	15.90	4.1
0.150 M	36.10	48.20	15.70	3.3

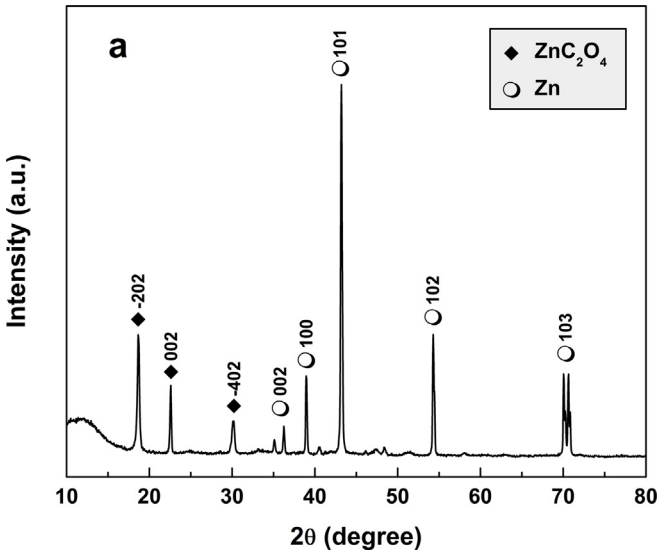

Fig. 7. XRD diffraction patterns of samples, polarized in: (a) 0.005, (b) 0.060 and (c) 0.150 M $H_2C_2O_4$, (5 mA cm^{-2}).

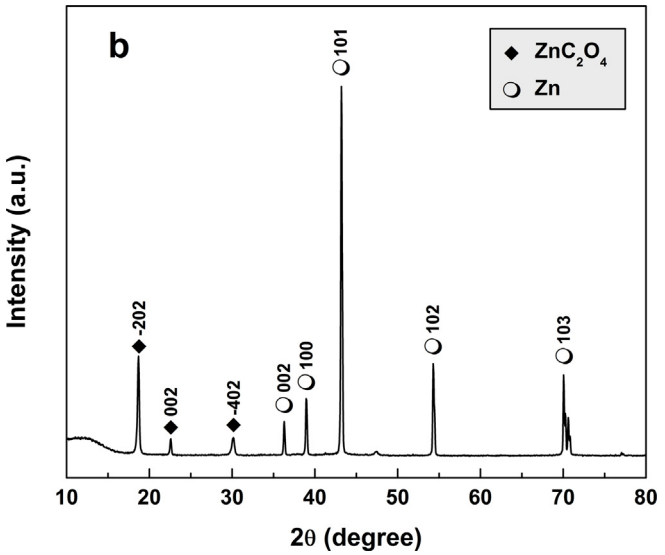

Fig. 7. (*continued*)

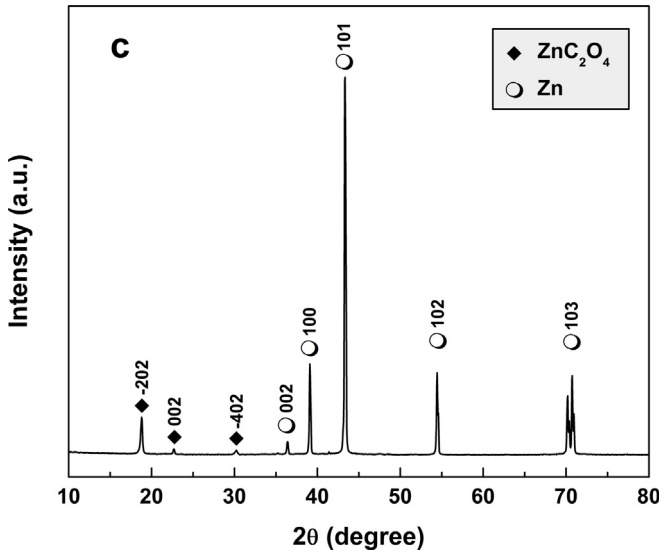

Fig. 7. (*continued*)

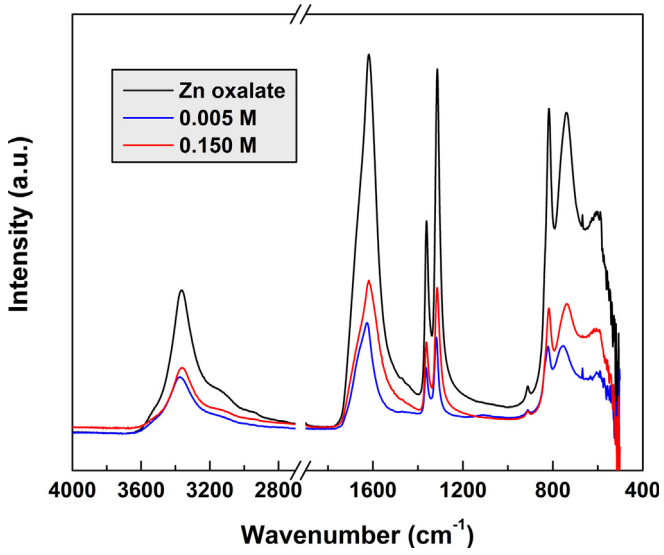

Fig. 8. ATR-FTIR spectra of samples anodically polarized in two oxalic acid solutions and referent pure Zn oxalate dihydrate in the region 4000 - 400 cm^{-1}..

The nucleation of the Zn-oxalate dihydrate crystals occurs at the very beginning of the anodic polarization (Fig. 9, position (a)). In the following stages, the already formed crystals grow gradually (Fig. 9, position (b)), occupying increasingly larger metallic surface areas. The polarization voltage remains almost unchanged during the entire induction period. This is due to the remaining of uncovered metallic surface areas, which provide direct contact with the electrolyte. The gradual decrement of the accessible bare metallic surface due to its occupation by the growing oxalate crystals does not affect the current as a galvanostatic regime is applied. However, the contact area decrement among the crystals is efficiently compensated by proportional the current density rise. Consequently, the higher current densities should lead to crystal growth acceleration, driven by the more intensive current flows through the remaining restricted unoccupied accessible areas. Nevertheless, especially at lower oxalic acid concentrations, the acceleration in crystal growth is being hindered by the more intensive consumption of oxalate ions on the metallic surface. Consequently, the process becomes diffusion-limited and its rate depends on the delivery of oxalate ions to the metallic surface.

The crystal growth process continues until the blockage of the entire sample surface with the already continuous oxalate film (c). This namely is the end of the induction period, which can easily be identified with the sharp increase in U_f (position d).

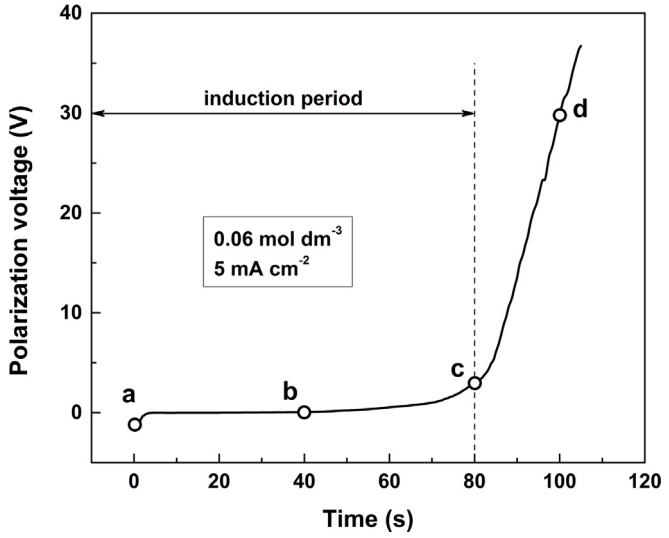

Fig. 9. Evolution of the formation voltage with the anodic polarization time.

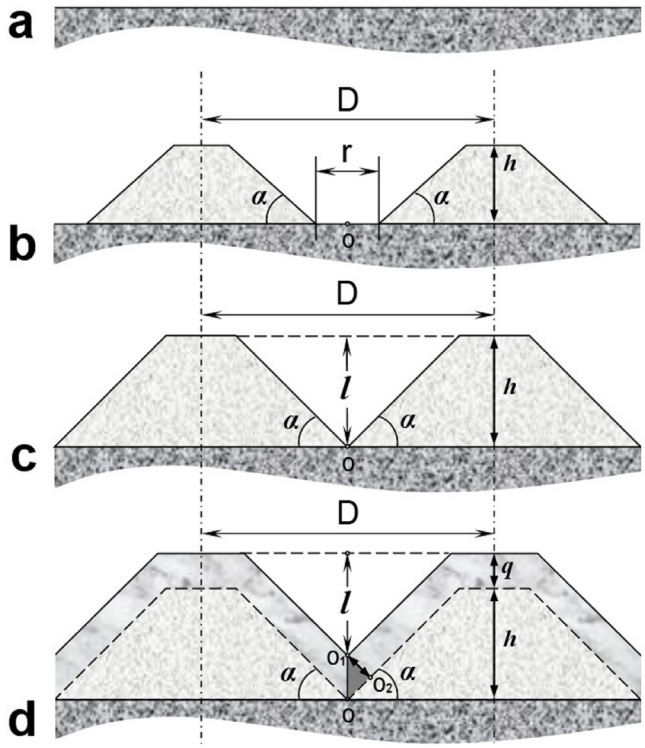

Fig. 10. Schematic presentation of $ZnC_2O_4.2H_2O$ film growth: (a) polished Zn surface, (b) during the induction period, (c) at the end of induction period and (d) after induction period.

If it is assumed that the shapes of the obtained crystallites resemble truncated pyramids, then a conceptual model describing the appearance of the observed induction periods could be created (Fig. 10).

When a polished Zn surface (a) is submitted to polarization, the nucleation of crystallites is immediately initiated (b). Their further growth causes a gradual occupation of larger surface areas, as already mentioned. In Fig. 10 the distance between two adjacent crystal nuclei is denoted with "D", the distance between vicinal growing crystallites during the induction period is given with "*r*", whereas their height is denominated by "*h*". The symbol "*l*" is ascribed to the resulting film roughness height. The crystal growth during the induction period is coincided by a gradual decrease of *r*, and an increase of *h*. The induction period completes (c) at the moment when the *r* value becomes $r = 0$. This moment is related to the maximal achievable *h* value. The end of the induction period indicates the complete coverage of the Zn-metallic surface with hydrated Zn-oxalate crystallites (i.e. formation of a consistent film). The induction period is followed by a sharp rise in the formation voltage (d). After this moment, the thickness of the already formed oxalate layer becomes $(h + q)$, and continues its increase, with the simultaneous decrease of *l*. This film roughness decrement is a result of the overlapping of the crystallites due to their continuous expansion. The sharp change in the $U_f(t)$–slope registered at the end of the induction periods is an indication for an increase in the polarization resistance of the samples, due to the thickening of the Zn-oxalate film. This results in the appearance of new geometrical measure *q*, which can be attributed to the truncated pyramides' expansion. The continuous increase of its values leads to a sharp rise of the resulting electric resistance and to a complete obstruction of the electrolyte access to the metallic surface.

The higher concentrations of the oxalic acid (a basic precursor for the formation of ZnC_2O_4) result in acceleration of the electrochemical Zn-oxalate formation reaction. Considering its heterogeneous character, it is easy to assume that the higher concentration of the precursor results in more intensive nucleation during the induction periods. In other words, the higher electrolyte concentration leads to the appearance of more nuclei per unit surface area. Hence, the larger number of these oxalate nuclei predetermine lower distances (denoted with "*r*" in the model) between them. Namely, this is the cause for the shorter induction periods and the finer grain structures of the resulting films, synthesized at higher oxalic acid concentrations.

Thus in the present case, the oxalate synthesis and the formation of the obtained films are not spontaneous processes, but rather these are driven by the current values, predetermined by the galvanostatic conditions. Consequently, the higher current densities predetermine much more intensive nucleation. Therefore, simultaneous nucleation of a larger number of nuclei will be observed. These nuclei will predetermine lower distances between them, which in turn supposes shorter induction periods, until the complete coverage of the substrate surface, which finally results in film morphology with finer grains.

Consequently, both the higher precursor concentrations and the applied higher currents will shorten the duration of the induction periods. The variation of these process parameters does not affect the composition and structure of the obtained films. As commented in section (3.2.2) crystalline Zn-oxalate structures were established with certainty in all investigated cases.

3.3.2. SEM morphological observations and model verification

Zn-samples anodized for different durations were observed using SEM in the respective stages of polarization (a-d), represented in the conceptual model. The obtained micrographs are represented in Fig. 11.

The comparison of the morphologies observed by SEM, reveals coverage of the fine grained bare metallic surface (a) by coarse crystals, (b) which gradually grow (c), reaching rather large dimensions, exceeding 2–3 μm. Their number per unit of surface area decreases due to their already commented overlapping (d).

According to the conceptual model and the observed morphological transformations, the film roughness should increase during the entire induction period. After the end of the induction period, a subsequent roughness decrease should be observed. These assumptions were verified by performing systematical AFM observations.

3.3.3. AFM roughness determination

Three-dimesional AFM images of Zn samples, after anodic polarization corresponding to stages (a–d) are shown in Fig. 12.

The images in the Fig. 12, clearly demonstrate the transition of the obviously smooth substrate surface (a) to a morphology of equally distributed coarse formations, due to the nucleation of the Zn-oxalate film (b). Further, their size increases, as a result of nuclei growth (c),

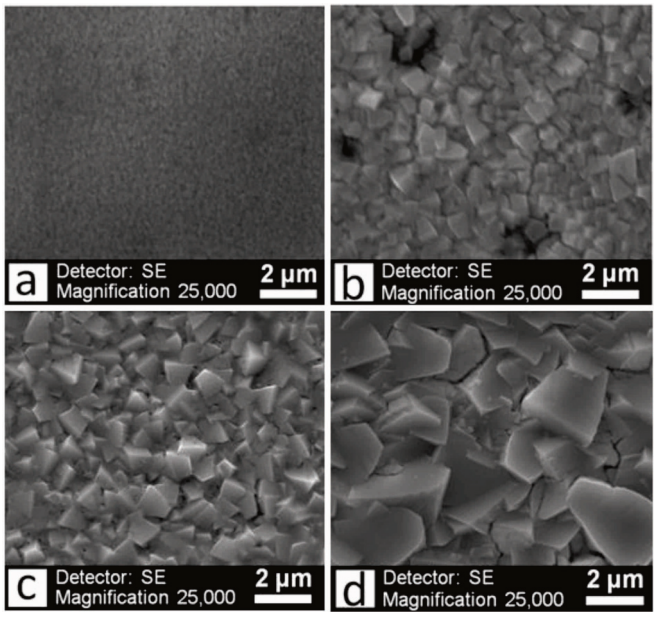

Fig. 11. SEM micrographs of the electrode surface at different stages (a–d) of anodic polarization.

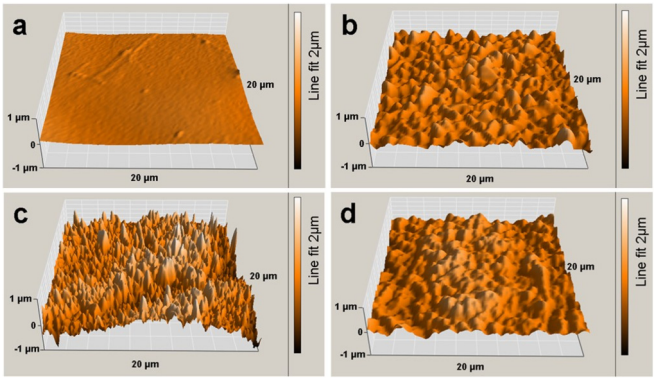

Fig. 12. 3D-AFM images of the investigated samples: (a) before the anodic polarization, (b) during the induction period, (c) at the end of the induction period and (d) after this period.

Table 2
Roughness parameters at different polarization stages.

Position	S_a (nm)	S_q (nm)	S_y (nm)	S_P (nm)	S_v (nm)	S_m (pm)
a	7.88	10.70	123.96	82.53	−41.43	213.34
b	88.52	113.86	947.59	580.93	−366.66	213.49
c	110.47	140.50	979.75	573.90	−405.85	185.88
d	68.76	86.82	617.03	356.44	−260.59	213.14

corresponding to an increase in the values of $l \approx h$, represented in the graphical model. The final morphology of the formed integral film after the induction period (d) resembles this of (b), the cause of which is the overlapping of the crystals. This leads to a decrease in the l values, compensated by the appearance and thickening of q, due to vicinal crystals overlapping. Indeed, the roughness increment during the entire induction period, followed by obvious smoothening was confirmed and registered by the quantitative analysis of the roughness parameters, summarized in Table 2.

The above table contains the following six basic statistical roughness measures: S_a (average roughness value) is the average sum of the module of distances of all points from the measured surface, in direction, perpendicular to the conditional plane; S_q (square root roughness value), defined as square root of the second power of S_a; S_m (mean roughness value) is also defined by the same average sum, but in this case, the respective positive (upward) or negative (downward) signs of the vectors are taken into account; S_v (valley depth) notes the distance between the conditional plane and the lowest point of the measured surface; S_p (peak height) is the distance between the highest point of the measured surface and the conditional plane; S_y (peak-valley height) is the distance between the highest (S_p), and the lowest (S_v) points of the measured surface.

The acquired results obviously show that the obtained films roughness increases during the entire induction period (a-c). The most significant parameter S_y, relevant to l in the proposed graphical model increases with almost an entire order of magnitude from 0.1 to 0.9 μm during the induction period. Afterwards, its value has an insignificant further growth, due to the considerable growth of the resistance, caused by the appearance and further increase of the parameter q. After the induction period, the S_y, parameter restores its values, revealing a smoothening of the already formed film. This subsequent smoothening is a result of the growing rate of crystal overlapping, which reduces the l value (associated with the height of the triangles, formed between adjacent truncated pyramids in the proposed graphical model). Thus, their expansion results in widening, which in turn causes a decrease of the size dimensions of the triangular spaces among the crystallite surfaces.

A subsequent decrease in l, at the further polarization stages (d) is registered. This ascertainment confirms the above proposed conceptual model for the explication of the appearance of the observed distinguishable induction periods in the case of anodic polarization of Zn in oxalic acid electrolytes.

The increase in roughness with thickness is a common behavior, coinciding the formation of thin films [73–77]. Nevertheless, in some cases [73,75] a slight roughness decrement was observed after the initial increase, caused by the expansion of the crystallites and their subsequent overlap.

3.4. Number and size of crystallites

The number of crystallites formed per unit surface area (cm^{-2}), at the end of the induction periods was determined by use of "ImageJ" software. The number of crystallites as a function of oxalic acid concentration is illustrated in Fig. 13.

The obtained results clearly indicate that during the polarization process, the number of nucleated crystallites (n) decreases, while their size (L) grows. It is worth noting that the number of crystallites at the

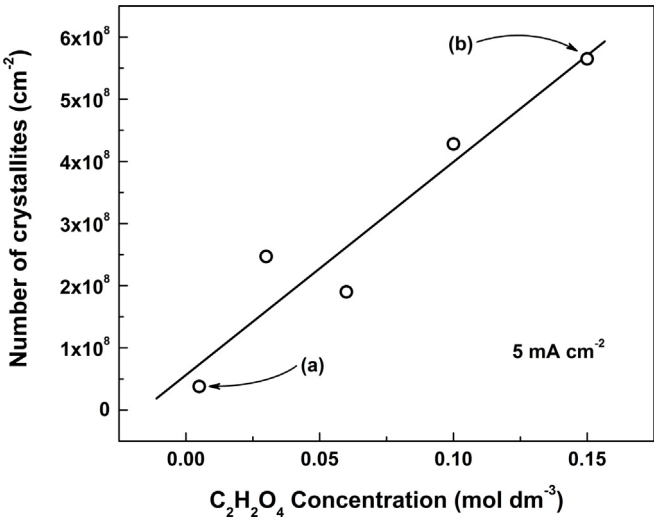

Fig. 13. Number of crystallites per unit surface area determined at the end of the induction period as a function of the electrolyte concentration.

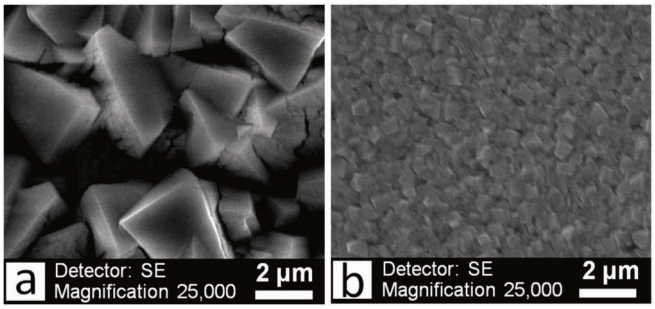

Fig. 14. SEM micrographs of Zn-foil sample surfaces after polarization in: (a) 0.005 M ($\tau_{ind} = 420\ s$) and (b) 0.150 M ($\tau_{ind} = 24\ s$) oxalic acid.

end of the induction period is relatively lower in the cases of diluted electrolytes (Figs. 13a and 14a), whereas their size is larger, compared to those formed in more concentrated electrolytes (Figs. 13b and 14b).

The obtained results clearly indicate that during the polarization process, the number of nucleated crystallites (n) decreases, while their size (L) grows.

The SEM micrographs present the electrode surfaces after the end of the induction periods for Zn-polarization in 0.005 M (a) and 0.150 M (b) oxalic acid (at 5 mA cm^{-2}).

The fact that the number and size of the formed Zn oxalate dihydrate crystallites depend on the concentration of oxalic acid explains the established decrement of the duration of the induction periods duration with increase of the oxalic acid concentration.

4. Conclusion

The present research shows the results of extended systematical elucidation of the zinc behavior during anodic polarization in oxalic acid solutions in a relatively wide interval of oxalic acid concentrations (from 0.005 to 0.500 M) and for a broad range of current densities (from 1.25 to 40.00 mA cm^{-2}).

The *in-situ* $U_f(t)$-kinetic curves have shown the occurrence of distinguishable induction periods. Their duration (τ_{ind}) is strongly dependent on both the acid concentration and the applied current densities, during the galvanostatic polarization experiments. These durations are considerable in the lower concentration range and sharply decay at higher oxalic acid concentrations. These induction periods become independent on the content of oxalic acid in the higher concentration range. Similar correlations were established regarding the impact of the applied current densities on (τ_{ind}). Besides, the longer induction periods, recorded at lower acid concentrations and at lower current densities reveal more notable dissipations, caused by the stochastic character of the film nucleation.

After the entire surface is covered, the voltages required for overcoming the films' resistances acquire significant values, exceeding 100 V in some cases.

All the specimens were submitted to systematic compositional (XPS) and structural (XRD and ATR-FTIR) analyses, combined with morphological (SEM) and topographical (AFM) observations.

The XPS analyses have shown that the formed films are covered with ZnO layers, whereas the XRD spectra have revealed the obtained films bulks are composed of crystalline $ZnC_2O_4.2H_2O$. This contradiction in the results of these analyses is a consequence of their different penetration depths. Nevertheless, the additional ATR-FTIR analysis has confirmed the statements made from the analysis of the XRD patterns.

The data analysis of the above mentioned methods, has served as a basis for the development of a graphical model regarding the Zn-oxalate film formation kinetics and mechanism at galvanostatic conditions. Further, this model was successfully used for the description of the causes for the occurrence of the observed induction periods and the attributed correlations of their durations with the oxalic acid concentrations and applied current densities. In addition, this model was also applied for the explication of the rather high voltages reached after the film formation.

Finally, the model's concepts were verified with supplemental SEM observations of each of the stages of film formation and the corresponding morphological (by coarse crystals nucleation and growth) and topographical alterations (by roughness increase and subsequent decrement due to crystal overlapping).

The model could successfully be applied in various research activities, devoted to the zincate corrosion protection improvement, Zn-based functional layers and optically active sensor elements.

Acknowledgements

The authors gratefully acknowledge the financial support from the Bulgarian National Scientific Fund under Project DM 19/6 (2017).

References

[1] S.-H. Cho, S.-J. Kim, W.-J. Jeong, S.-H. Kim, Electrical, optical, and electrochemical corrosion resistance properties of aluminum-doped zinc oxide films depending on the hydrogen content, J. Korean Inst. Surf. Eng. 51 (2018) 116–125.
[2] L. Zhang, M. Jeem, K. Okamoto, S. Watanabe, Photochemistry and the role of light during the submerged photosynthesis of zinc oxide nanorods, Sci. Rep. 8 (2018) 1–13.
[3] L.D. Trino, L.F.G. Dias, L.G.S. Albano, E.S. Bronze-Uhle, E.C. Rangel, C.F.O. Graeff, P.N. Lisboa-Filho, Zinc oxide surface functionalization and related effects on corrosion resistance of titanium implants, Ceram. Int. 44 (2018) 4000–4008.
[4] K. Kamburova, N. Boshkova, N. Boshkov, G. Atanassova, T. Radeva, Hybrid zinc coatings for corrosion protection of steel using polyelectrolyte nanocontainers loaded with benzotriazole, Colloids Surf., A 559 (2018) 243–250.
[5] J. Yuan, R. Yuan, J. Wang, Q. Li, X. Xing, X. Liu, W. Hu, Fabrication and corrosion resistance of phosphate/ZnO multilayer protective coating on magnesium alloy, Surf. Coating. Technol. 352 (2018) 74–83.
[6] Z. Sharifalhoseini, M.H. Entezari, M. Shahidi, Sonication affects the quantity and the morphology of ZnO nanostructures synthesized on the mild steel and changes the corrosion protection of the surface, Ultrason. Sonochem. 41 (2018) 492–502.
[7] Z. Sharifalhoseini, M.H. Entezari, M. Shahidi, Synergistic effect of low and high intensity ultrasonic irradiation on the direct growth of ZnO nanostructures on the galvanized steel surface: investigation of the corrosion behavior, Ultrason. Sonochem. 44 (2018) 380–389.
[8] M. Peshova, V. Bachvarov, St Vitkova, G. Atanasova, N. Boshkov, Electrodeposited zinc composite coatings with embedded carbon nanotubes – advanced composite materials for better corrosion protection, Trans. IMF 96 (2018) 324–331.
[9] S. Kuang, W. Zheng, Y. Gu, Z. Sun, Z. Yang, W. Li, C. Feng, Dual-functional $Zn_xMg_{1-x}O$ solid solution nanolayer modified ZnO tussock-like nanorods with improved photoelectrochemical anti-corrosion performance, J. Electroanal. Chem. 815 (2018) 175–182.
[10] I.O. Arukalam, M. Meng, H. Xiao, Y. Ma, E.E. Oguzie, Y. Li, Effect of perfluorodecyltrichlorosilane on the surface properties and anti-corrosion behavior of poly(dimethylsiloxane)-ZnO coatings, Appl. Surf. Sci. 433 (2018) 1113–1127.
[11] L. Peng, H. Hong, Y. Shi, X. Zhou, Y. Lin, J. Jia, High performance CdSe quantum dot sensitized ZnO solar cell fabricated from ion exchange, J. Alloy. Comp. 765 (2018) 355–361.
[12] Z. Zang, Efficiency enhancement of ZnO/Cu_2O solar cells with well oriented and micrometer grain sized Cu_2O films, Appl. Phys. Lett. 112 (2018) 042106.
[13] K. Mahmood, A. Khalid, M.T. Mehran, Nanostructured ZnO electron transporting materials for hysteresis-free perovskite solar cells, Sol. Energy 173 (2018) 496–503.
[14] S.K. Kokate, A.T. Supekar, P.K. Baviskar, B.M. Palve, Sandesh, R.J. Kakasahe, C. Mohite, H.M. Pathan, CdS sensitized pristine and Cd doped ZnO solar cells: effect of SILAR cycles on optical properties and efficiency, Mater. Sci. Semicond. Process. 80 (2018) 179–183.
[15] S. Zhuang, M. Lu, N. Zhou, L. Zhou, D. Lin, Z. Peng, Q. Wu, Cu modified ZnO nanoflowers as photoanode material for highly efficient dye sensitized solar cells, Electrochim. Acta 294 (2018) 28–37.
[16] Z. Qiao, C. Xia, Y. Cai, M. Afzal, H. Wang, J. Qiao, B. Zhu, Electrochemical and electrical properties of doped CeO_2-ZnO composite for low-temperature solid oxide fuel cell applications, J. Power Sour. 392 (2018) 33–40.
[17] J. Zhang, H. Song, R. Xu, C. Yan, Y. Wu, The heterogeneous electrolyte of $CuFeO_2$ nano-flakes composited with flower-shaped ZnO for advanced solid oxide fuel cells, Int. J. Hydrogen Energy 43 (2018) 12789–12796.
[18] C. Xia, Z. Qiao, L. Shen, X. Liu, Y. Cai, Y. Xu, J. Qiao, H. Wang, Semiconductor electrolyte for low-operating-temperature solid oxide fuel cell: Li-doped ZnO, Int. J. Hydrogen Energy 43 (2018) 12825–12834.
[19] K. Thirumalai, M. Shanthi, M. Swaminathan, Highly active rare earth (RE) vanadate, tungstate loaded ZnO (RE= Gd, Dy and Ho) nanocomposites for electrochemical methanol oxidation-A comparative study for fuel cell application, Mater. Today 5 (2018) 15342–15347.
[20] Y.-H. Zhang, C.-Y. Liu, B.-B. Jiu, Y. Liu, F.-L. Gong, Facile synthesis of Pd-decorated ZnO nanoparticles for acetone sensors with enhanced performance, Res. Chem.

Intermed. 44 (2018) 1569–1578.
[21] M.M. Arafat, J.Y. Ong, A.S.M.A. Haseeb, Selectivity shifting behavior of Pd nanoparticles loaded zinc stannate/zinc oxide (Zn_2SnO_4/ZnO) nanowires sensors, Appl. Surf. Sci. 435 (2018) 928–936.
[22] J. Xu, S. Li, L. Li, L. Chen, Y. Zhu, Facile fabrication and superior gas sensing properties of spongelike Co-doped ZnO microspheres for ethanol sensors, Ceram. Int. 44 (2018) 16773–16780.
[23] Z. Shen, X. Zhang, R. Mi, M. Liu, Y. Chen, C. Chen, S. Ruan, On the high response towards TEA of gas sensors based on Ag-loaded 3D porous ZnO microspheres, Sens. Actuators, A 270 (2018) 492–499.
[24] B. Renganathan, D. Sastikumar, G. Gobi, N.R. Yogamalar, A.C. Bose, Nanocrystalline ZnO coated fiber optic sensor for ammonia gas detection, Optic Laser. Technol. 43 (2018) 1398–1404.
[25] J.R. Neal, A.J. Behan, R.M. Ibrahim, H.J. Blythe, M. Ziese, A.M. Fox, G.A. Gehring, Room-temperature magneto-optics of ferromagnetic transition-metal-doped ZnO thin films, Phys. Rev. Lett. 96 (2006) 197208.
[26] N.A. Yebo, P. Lommens, Z. Hens, R. Baets, An integrated optic ethanol vapor sensor based on a silicon-on-insulator microring resonator coated with a porous ZnO film, Optic Express 18 (2010) 11859–11866.
[27] A.J. Jafari, R.R. Kalantary, A. Esrafili, H. Arfaeini, Synthesis of silica-functionalized graphene oxide/ZnO coated on fiberglass and its application in photocatalytic removal of gaseous benzene, Process Saf. Environ. Protect. 116 (2018) 377–387.
[28] A.J. Jafari, H. Arfaeini, M.Y. Badi, R.R. Kalantary, M. Kermani, Ozone-Assisted photocatalytic degradation of benzene using nano-zinc oxide impregnated granular activated carbon (ZnO–GAC) in a continuous fluidized bed reactor, Environ. Prog. Sustain. Energy (2018) 1–3 https://doi.org/10.1002/ep.13082.
[29] C. Nie, L. Liu, R. He, Pt/TiO_2-ZnO in a circuit Photo-electro-catalytically removed HCHO for outstanding indoor air purification, Separ. Purif. Technol. 206 (2018) 316–323.
[30] A. Changsuphan, N.T.K. Oanh, Catalytic oxidation of volatile organic compounds by 13X zeolite coated with nZnO in presence of UV and ozone at high bed temperature, Water Air Soil Pollut. 229 (2018) 1–14.
[31] L. Zaraska, K. Mika, K. Syrek, G.D. Sulka, Formation of ZnO nanowires during anodic oxidation of zinc in bicarbonate electrolytes, J. Electroanal. Chem. 801 (2017) 511–520.
[32] A. Kaleva, J.-P. Nikkanen, S. Heinonen, V. Saarimaa, T. Vuorinen, M. Honkanen, L. Hyvärinen, E. Levänen, Synthesis of ZnO nanowires with supercritical carbon dioxide and post heat treatment, Nanotechnology 29 (2018) 445601.
[33] L. Zaraska, K. Mika, K.E. Hnida, M. Gajewska, T. Łojewski, M. Jaskuła, G.D. Sulka, High aspect-ratio semiconducting ZnO nanowires formed by anodic oxidation of Zn foil and thermal treatment, Mater. Sci. Eng. B 226 (2017) 94–98.
[34] S.S. Chang, S.O. Yoon, H.J. Park, A. Sakai, Luminescence properties of anodically etched porous Zn, Appl. Surf. Sci. 158 (2000) 330–334.
[35] A.R.S. Kannan, S. Muralidharan, K.B. Sarangapani, V. Balaramachandran, V. Kapali, Corrosion and anodic behaviour of zinc and its ternary alloys in alkaline battery electrolytes, J. Power Sour. 57 (1995) 93–98.
[36] N.A. Hampson, P.E. Shawt, R. Taylor, Anodic behaviour of zinc in potassium Hydroxide Solution: II.* Horizontal anodes in electrolytes containing Zn(II), Br. Corrosion J. 4 (1969) 207–211.
[37] J. Park, K. Kim, J. Choi, Formation of ZnO nanowires during short durations of potentiostatic and galvanostatic anodization, Curr. Appl. Phys. 13 (2013) 1370–1375.
[38] F. Touri, A. Sahari, A. Zouaoui, F. Deflorian, Detection and characterization of ZnO on a passive film of pure zinc, Int. J. Electrochem. Sci. 12 (2017) 10813–10823.
[39] X. Wu, G. Lu, C. Li, G. Shi, Room-temperature fabrication of highly oriented ZnO nanoneedle arrays by anodization of zinc foil, Nanotechnology 17 (2006) 4936–4940.
[40] M. Shamsipur, M. Roushani, S.M. Pourmortazavi, Electrochemical synthesis and characterization of zinc oxalate nanoparticles, Mater. Res. Bull. 48 (2013) 1275–1280.
[41] M.A. Imam, M. Moniruzzaman, M.A. Mamun, Anodizing of zinc for improved surface properties, *Proceeds.* 18th International Corrosion Congress. Perth, Australia. 20-24, vol. 1, November 2011, pp. 199–206.
[42] A. Shetty, K.K. Nanda, Synthesis of zinc oxide porous structures by anodization with water as an electrolyte, Appl. Phys. A 109 (2012) 151–157.
[43] J. Światowska-Mrowiecka, J. Bana, Anodic behaviour of zinc in methanol solutions of lithium perchlorate, Electrochim. Acta 50 (2005) 1829–1840.
[44] S.J. Kim, J. Choi, Self-assembled arrays of ZnO stripes by anodization, Electrochem, Commun. Now. 10 (2008) 175–179.
[45] N.K. Shrestha, R. Hahn, K. Lee, A. Tighineanu, P. Schmuki, Electrochemically assisted self-assembling of ZnF_2–ZnO nanospheres: formation of hierarchical thin porous films, ECS Electrochem. Lett. 3 (2014) E1–E3.
[46] S.S. Chang, S.O. Yoon, H.J. Park, A. Sakai, Luminescence properties of Zn nanowires prepared by electrochemical etching, Mater. Lett. 53 (2002) 432–436.
[47] S.J. Kim, J. Lee, J. Choi, Understanding of anodization of zinc in an electrolyte containing fluoride ions, Electrochim. Acta 53 (2008) 7941–7945.
[48] N. Beedri, Y. Inamdar, S.A. Sayyed, A. Shaikh, S. Jadkar, H. Pathan, Growth of Zinc oxide porous films via electrochemical anodization using glycerol based electrolyte, Chemistry and Chemical Technology 8 (2014) 283–286.
[49] S. Jakobson, D. Crotty, R. Griffin, D. Phipps, Zinc Anodizing, Metal Finishing. 96 (1998) 114–118.
[50] M. Remešová, L. Klakurková, M. Horynová, L. Čelko, Preparation of metallographic samples with anodizing layers, Mater. Sci. Forum 891 (2017) 106–110.
[51] A. Ravanbakhsh, F. Rashchi, M.H. Sohi, R.K. Nekouei, M.M. Samarin, Synthesis and characterization of porous zinc oxide nano-flakes film in alkaline media, J. Ultrafine Grained Nanostruct. Mater. 51 (2018) 32–42.
[52] P.K. Basu, N. Saha, S. Maji, H. Saha, S. Basu, Nanoporous ZnO thin films deposited by electrochemical anodization: effect of UV light, J. Mater. Sci. 19 (2008) 493–499.
[53] P.K. Basu, E. Bontempi, S. Maji, H. Saha, S. Basu, Variation of optical band gap in anodically grown nanocrystalline ZnO thin films at room temperature - effect of electrolyte concentrations, J. Mater. Sci. 20 (2009) 1203–1207.
[54] S. Gilani, M. Ghorbanpour, A.P. Jadid, Antibacterial activity of ZnO films prepared by anodizing, J. Nanostruc. Chem. 6 (2016) 183–189.
[55] I. Angelov, E. Klein, A. Girginov, S. Ikonopisov, Comparative studies of induction periods during anodization, C. R. Acad. Bulg. Sci. 43 (1990) 61–64.
[56] S. Ikonopisov, Ts Nikolov, High resistance anodic film formation on bismuth with or without appearance of induction period, J. Electrochem. Soc. 119 (1972) 1544–1550.
[57] M. Bojinov, I. Kanazirski, A. Girginov, Anodic film growth on antimony in H_3PO_4 solutions, Electrochim. Acta 40 (1995) 873–878.
[58] S. Ikonopisov, Anodization of molybdenum in glycol-borate electrolyte - a peculiar kinetics of insulating film formation, Electrodepos. Surf. Treat. 1 (1973) 305–317.
[59] A.G. Gad-Allah, H.A. Abd El-Rahman, Anodization of molybdenum. I. Galvanostatic anodization, J. Appl. Electrochem. 17 (1987) 1065–1074.
[60] S. Nishikida, S. Ikeda, Studies on the chemical shifts of auger electron energies for magnesium and zinc in their compounds, Bull. Chem. Soc. Jpn. 51 (1978) 154–158.
[61] M.C. Biesinger, L.W.M. Lau, A.R. Gerson, R. St, C. Smart, Resolving surface chemical states in XPS analysis of first row transition metals, oxides and hydroxides: Sc, Ti, V, Cu and Zn, Appl. Surf. Sci. 257 (2010) 887–898.
[62] E.C. Onyiriuka, Zinc phosphate glass surfaces studied by XPS, J. Non-Cryst. Solids 163 (1993) 268–273.
[63] L.G. Mar, P.Y. Timbrell, R.N. Lamb, An XPS study of zinc oxide thin film growth on copper using zinc acetate as a precursor, Thin Solid Films 223 (1993) 341–347.
[64] A. Ganguly, S. Sharma, P. Papakonstantinou, J. Hamilton, Probing the thermal deoxygenation of graphene oxide using high-resolution in situ X-ray-based spectroscopies, J. Phys. Chem. C 115 (2011) 17009–17019.
[65] P. Benjwal, M. Kumar, P. Chamoli, K.K. Kar, Enhanced photocatalytic degradation of methylene blue and adsorption of arsenic(III) by reduced graphene oxide (rGO)–metal oxide (TiO_2/Fe_3O_4) based nanocomposites, RSC Adv. 5 (2015) 73249–73260.
[66] M. Jin, H.-K. Jeong, T.-H. Kim, K.P. So, Y. Cui, W.J. Yu, E.J. Ra, Y.H. Lee, Synthesis and systematic characterization of functionalized graphene sheets generated by thermal exfoliation at low temperature, J. Phys. D Appl. Phys. 43 (2010) 275402.
[67] R. Deyrieux, C. Berro, A. Peneloux, Crystal structure of two allotropic forms of dihydrated ferrous oxalate, Bull. Soc. Fr. Mineral. Cristal. 1 (1973) 25–34.
[68] JCPDS, International Centre for Diffraction Data PCPDFWIN 2.2 (2001).
[69] http://webbook.nist.gov/cgi/cbook.cgi?ID=B6000060&Mask=80#IR-Spec.
[70] N.D. Cooper, Kinetic and mechanistic study of the decomposition of zinc oxalate, Proceed: National Conference on Undergraduate Research (NCUR), Eastern Washington University, Cheney WA, 2015, p. 292. April 16-18.
[71] C. Hu, J. Mi, S. Suli, J. Shangguan, The study of thermal decomposition kinetics of zinc oxide formation from zinc oxalate dehydrate, J. Therm. Anal. Calorim. 115 (2014) 1119–1125.
[72] A. Wladimirsky, D. Palacios, M.C. D'Antonio, A.C. Gonzalez-Baro, E.J. Baran, Vibrational spectra of the α-$M^{II}C_2O_4.2H_2O$ oxalate complexes, with M^{II} = Co, Ni, Zn, An. Asoc. Quim. Argent 98 (2011) 71–77.
[73] Y. Cao, C. Zhou, Thickness dependence of surface roughness and magnetic properties of FeNiCr thin films, J. Magn. Magn Mater. 333 (2013) 1–7.
[74] Z. Xin, S. Xiao-Hui, Z. Dian-Lin, Thickness dependence of grain size and surface roughness for dc magnetron sputtered films, Chin. Phys. B19 (2010) 86801–86802.
[75] Y.S. Yoon, W.N. Kang, S.S. Yom, Substrate and thickness dependence of surface morphology and roughness of superconducting $Y_1Ba_2Cu_3O_{7-x}$ thin films, Adv. Supercond. 6 (1994) 1023–1026.
[76] V. Kapaklis, P. Poulopoulos, V. Karaoutsos, Th Manouras, C. Politis, Growth of thin Ag films produced by radiofrequency magnetron sputtering, Thin Solid Films 510 (2006) 138–142.
[77] D. Hong, Y.R. Do, H.T. Kwak, S. Yim, Structural templating and growth behavior of copper phthalocyanine thin films deposited on a polycrystalline perylenetetracarboxylic dianhydride layer, J. Appl. Phys. 109 (2011) 063507 https://doi.org/10.1063/1.3553884.